J Mol Model (2010) 16:1679–1691
DOI 10.1007/s00894-010-0692-x

ORIGINAL PAPER

Quantitative analysis of molecular surfaces: areas, volumes, electrostatic potentials and average local ionization energies

Felipe A. Bulat · Alejandro Toro-Labbé · Tore Brinck · Jane S. Murray · Peter Politzer

Received: 9 November 2009 / Accepted: 3 February 2010 / Published online: 2 April 2010

Abstract We describe a procedure for performing quantitative analyses of fields $f(\mathbf{r})$ on molecular surfaces, including statistical quantities and locating and evaluating their local extrema. Our approach avoids the need for explicit mathematical representation of the surface and can be implemented easily in existing graphical software, as it is based on the very popular representation of a surface as collection of polygons. We discuss applications involving the volumes, surface areas and molecular surface electrostatic potentials, and local ionization energies of a group of 11 molecules.

F. A. Bulat (✉)
Fable Theory & Computation LLC,
PO Box 21811,
Washington DC 20009, USA
e-mail: fbulat@fabletc.com
e-mail: fbulat@puc.cl

A. Toro-Labbé
Laboratorio de Química Teórica Computacional (QTC),
Facultad de Química, Pontificia Universidad Católica de Chile,
Vicuña Mackenna 4860, Macul,
Santiago, Chile

T. Brinck
Physical Chemistry, School of Chemical Science and Engineering,
Royal Institute of Technology (KTH),
SE-100 44 Stockholm, Sweden

J. S. Murray · P. Politzer
Department of Chemistry, University of New Orleans,
New Orleans, LA 70148, USA

J. S. Murray · P. Politzer
CleveTheoComp,
1951 W. 26th Street,
Cleveland, OH 44113, USA

Keywords Generation and analysis of molecular surfaces · Electrostatic potential · Average local ionization energy · Volume · Surface area

Introduction

Molecular surfaces

The concept of a molecular surface is not a rigorous one, since the electronic density of a molecule extends, in principle, to infinity. In practice, however, it is a very useful concept. For example, knowledge of the energetic and electrostatic features on an appropriately defined surface of a molecule can provide insight into its interactions with other molecules—the subject of the present paper. Furthermore, an encompassing surface defines a volume, and molecule volumes are important for a variety of purposes, including predicting polarizabilities [1–3] and estimating the crystal densities [4–7] and impact sensitivities of energetic compounds [8].

A molecular surface has often been taken to be the exposed portions of the outer surfaces of a set of intersecting spheres centered at the positions of the individual nuclei [9–14]; these spheres are typically given the van der Waals radii of the respective atoms [15]. A refinement of this approach, intended to smooth over the intersections, is to roll a probe sphere over this entire surface, and let the final molecular surface be that traced out by either the edge or the center of the probe sphere. The latter can be assigned a radius corresponding to some solvent molecule, and the result is termed a "solvent-accessible surface." For more detailed discussions of these, and techniques for generating them, see Brickmann et al. [16] and Connolly [17].

A quite different basis for defining a molecular surface was proposed by Bader et al. [18, 19]: an outer contour of the molecule's electronic density $\rho(\mathbf{r})$, e.g. $\rho(\mathbf{r})$=0.001 or 0.002 a.u. (electrons/bohr^3). This has the advantage over the intersecting sphere model that it reflects features specific to the particular molecule, such as lone pairs, π electrons, the presence of σ-holes [20], etc. It has been demonstrated that these contours encompass 95–98% of a molecule's electronic density [12, 18, 19].

For some purposes, such as estimating molecular volumes, the choice of the outer contour clearly makes a significant difference; thus, for the molecule $(H_2N)_2C{=}C(NO_2)_2$, the volume within the 0.001 a.u. contour is about 17% greater than that within the 0.002 a.u. On the other hand, for predicting molecules' reactive behaviors from the properties of the electrostatic potentials or local ionization energies on their surfaces, the same trends will be observed on any outer contour of $\rho(\mathbf{r})$, i.e. 0.001, 0.0015, 0.002 a.u., etc. [21, 22]. In this context, it is important to note that these three contours are normally beyond atomic van der Waals radii (except sometimes for that of hydrogen) [12, 23], so that these surfaces are indeed relevant to what an approaching entity "sees" prior to the beginning of interaction.

Our focus in this paper is on characterizing the electrostatic potentials and local ionization energies on molecular surfaces corresponding to outer contours of $\rho(\mathbf{r})$. We will begin with some background discussion of these two properties, and then will discuss the methodology for obtaining the molecular surfaces. We will describe our surface analysis algorithm and its computer implementation, with an emphasis on the quantitative characterization of molecular surfaces by means of several relevant descriptors.

Two key properties on molecular surfaces

A molecule's electrostatic potential $V(\mathbf{r})$ and average local ionization energy $\bar{I}(\mathbf{r})$ have proven to be effective guides to its reactive behavior. $V(\mathbf{r})$ is the potential that is created at any point $\mathbf{r}$ by the molecule's nuclei and electrons, and is given rigorously by,

$$V(\mathbf{r}) = \sum_A \frac{Z_A}{|\mathbf{R}_A - \mathbf{r}|} - \int \frac{\rho(\mathbf{r}')d\mathbf{r}'}{|\mathbf{r}' - \mathbf{r}|} \quad (1)$$

in which Z_A is the charge on nucleus A, located at $\mathbf{R}_A$, and $\rho(\mathbf{r})$ is the molecule's electronic density. $V(\mathbf{r})$ is a physical observable; it can be obtained experimentally, by diffraction methods [24, 25], as well as computationally. Its sign in any region of space depends upon whether the positive contribution of the nuclei or the negative one of the electrons is dominant there.

In contrast to $V(\mathbf{r})$, $\bar{I}(r)$ is a defined property [26], Eq. 2, although well-rooted in Hartree-Fock theory and Koopmans' theorem [27].

$$\bar{I}(\mathbf{r}) = \frac{\sum_i \rho_i(\mathbf{r})|\varepsilon_i|}{\rho(\mathbf{r})} \quad (2)$$

In Eq. 2, $\rho_i(\mathbf{r})$ is the electronic density of the i^{th} occupied atomic or molecular orbital and ε_i is its energy. $\bar{I}(\mathbf{r})$ is interpreted as the average energy needed to remove an electron at the point $\mathbf{r}$, the focus being upon the point in space rather than upon a particular orbital. While $\bar{I}(\mathbf{r})$ was introduced within the Hartree-Fock framework, it has been found to be equally useful in terms of Kohn-Sham density functional theory [28, 29]; the magnitudes are different but the trends are the same, which is the main issue in applications related to chemical reactivity. An interesting feature of $\bar{I}(\mathbf{r})$ is that it can be formally linked to $V(\mathbf{r})$ [29] and to the Fukui function [30].

In using $V(\mathbf{r})$ and $\bar{I}(\mathbf{r})$ to analyze and predict interactive behavior, they are generally evaluated on the molecular surface, and labeled $V_S(\mathbf{r})$ and $\bar{I}_S(\mathbf{r})$. These have been found to be complementary [31]. $V_S(\mathbf{r})$ is effective for noncovalent interactions, which are largely electrostatic in nature [32–34], while $\bar{I}_S(\mathbf{r})$ is more suitable when there is transfer of charge, bond formation, etc. For the applications of $V_S(\mathbf{r})$ and $\bar{I}_S(\mathbf{r})$ that are to be discussed in this section, we have previously used the HardSurf program [35] to obtain quantitative characterizations of these properties on molecular surfaces.

It might seem that $V_S(\mathbf{r})$ could also predict sites for electrophilic and nucleophilic bond-forming attack, by means of its most negative and positive regions. However $V_S(\mathbf{r})$ is not consistently reliable in this respect, because the regions of most negative $V_S(\mathbf{r})$ do not always correspond to the sites where the most reactive electrons are located. For example, the most negative $V_S(\mathbf{r})$ in benzene derivatives such as aniline, phenol, fluoro- and chlorobenzene, and nitrobenzene are associated with the substituents [31], whereas electrophilic reaction occurs on the rings. In contrast, $\bar{I}_S(\mathbf{r})$ correctly predicts the ortho/para- or meta-directing effects of the substituents, as well as their activation or deactivation of the ring [26, 28, 31]. This will be further discussed in relation to Fig. 5. On the other hand, the most positive and most negative values of $V_S(\mathbf{r})$, the $V_{S,max}$ and $V_{S,min}$, do correlate well, for molecules in general, with empirical measures of hydrogen-bond-donating and -accepting tendencies [36]; hydrogen bonding is of course a noncovalent interaction. More recently, it has been shown that $V_{S,max}$ found on the extensions of bonds involving Group IV–VII covalently-bonded atoms are indicative of the presence of positive σ-holes [20], and correlate with the computed interaction energies of these

sites with a given Lewis base [37]. Examples of positive σ-holes will be seen in Fig. 7.

The positive and negative extrema are just two of several quantities that help to characterize the detailed features of the electrostatic potential on a molecular surface. Others include its overall average value $\overline{V}_S$, its positive and negative averages $\overline{V}_S^+$ and $\overline{V}_S^-$, the average deviation Π, the positive, negative and total variances, σ_+^2, σ_-^2 and σ_{tot}^2, and an electrostatic balance parameter ν. These quantities are computed by appropriate summations over a finely spaced grid covering the entire molecular surface:

$$\overline{V}_S = \frac{1}{t}\sum_{i=1}^{t} V_S(\mathbf{r}_i) \quad \overline{V}_S^+ = \frac{1}{m}\sum_{j=1}^{m} V_S^+(\mathbf{r}_j) \quad \overline{V}_S^- = \frac{1}{n}\sum_{k=1}^{n} V_S^-(\mathbf{r}_k) \tag{3}$$

$$\Pi = \frac{1}{t}\sum_{i=1}^{t} \left| V_S(\mathbf{r}_i) - \overline{V}_S \right| \tag{4}$$

$$\sigma_{tot}^2 = \sigma_+^2 + \sigma_-^2 = \frac{1}{m}\sum_{j=1}^{m}\left[V_S^+(\mathbf{r}_j) - \overline{V}_S^+\right]^2 + \frac{1}{n}\sum_{k=1}^{n}\left[V_S^-(\mathbf{r}_k) - \overline{V}_S^-\right]^2 \tag{5}$$

$$\nu = \frac{\sigma_+^2\sigma_-^2}{\left(\sigma_+^2+\sigma_-^2\right)^2} \tag{6}$$

In these summations, t is the total number of points on the surface grid and m and n are the numbers of points at which $V_S(\mathbf{r})$ is positive, $V_S^+(\mathbf{r}_j)$, and negative, $V_S^-(\mathbf{r}_k)$, respectively.

Π is interpreted as an indicator of internal charge separation, which is present even in molecules having zero dipole moment due to symmetry, e.g. para-dinitrobenzene and boron trifluoride. It has been shown to correlate with empirical polarity scales [22, 38]. The variances—σ_+^2, σ_-^2 and σ_{tot}^2 —reflect the strengths and variabilities of the positive, negative and overall surface potentials [38]. Due to the terms being squared, they emphasize particularly the local extrema, the $V_{S,max}$ and $V_{S,min}$ (there may be several of each). Finally, the parameter ν is a measure of the degree of balance between the positive and negative potentials; when $\sigma_+^2 = \sigma_-^2$, ν has its maximum value of 0.25.

We have demonstrated that a variety of condensed-phase physical properties that depend upon noncovalent interactions can be expressed analytically in terms of various subsets of the quantities that have been defined. These properties include boiling and critical points, heats of phase transitions, solubilities and solvation energies, partition coefficients, liquid and solid densities, enzyme inhibition, viscosities, diffusion constants and surface tensions. This work has been reviewed on several occasions [38–41].

The features of $\bar{I}_S(\mathbf{r})$ could be characterized analogously to those of $V_S(\mathbf{r})$—its extrema, its average magnitude, average deviation and variance—keeping in mind that $\bar{I}_S(\mathbf{r})$ only has positive values. In the past, attention has focused primarily upon its local minima and, to a lesser extent, its average over the molecular surface. The lowest values of $\bar{I}_S(\mathbf{r})$, the $\bar{I}_{S,min}$, show the locations of the least tightly bound, most reactive electrons. Thus the $\bar{I}_{S,min}$ can be used to identify and rank sites susceptible to electrophilic attack [26, 28, 31], as will be seen below. $\bar{I}_{S,min}$ have also been demonstrated to correlate with basicities and proton affinities, and to reveal radical sites, double bond character and strained bonds. Other applications of $\bar{I}_S(\mathbf{r})$ related to molecular reactivity include local hardness and local polarizability. Detailed reviews have been given by Politzer et al. [42, 43].

Marching tetrahedra

In this section we shall begin by introducing the methods used to generate molecular surface representations and later describe some details of our implementation. We shall give enough detail so that the subsequent section ("Surface Analyses") follows naturally and can be understood without consulting the literature. The molecular surfaces are obtained through the Marching Tetrahedra (MT) algorithm [44] for isosurface extraction, which is based on the popular Marching Cubes (MC) algorithm [45]. Since being proposed more than two decades ago, these methods have been used widely in computer graphics for various fields, including Chemistry [46]. Our focus here is on its usage for quantitative characterization of molecular surfaces. As described in the following, the underlying surface representations obtained lend themselves naturally to quantitative analysis. We note that our analysis method can be implemented readily in chemical software that uses the MC or MT algorithm for visualization of molecular surfaces, or that generates equivalent surface representations.

A surface can be approximated by a series of polygons—whose vertices lie on the surface—joined together by their edges. For example, the great rhombicosidodecahedron or the truncated icosahedron ("buckyball") in Fig. 1 can be considered approximations of a sphere. The representation of arbitrary, non-regular surfaces by a collection of different kinds of polygons can become quite intricate because all the vertices of each polygon need to be coplanar (otherwise it cannot be represented by a planar patch in the shape of the polygon). The complexity of using polygons with arbitrary numbers of vertices can be avoided by using triangles only, because three vertices are guaranteed to be coplanar. A sphere could thus be approximated by triangles only; its surface has then been "triangulated". The more

Fig. 1 From *left* to *right*: The great rhombicosidodecahedron; the truncated icosahedron; a regularly triangulated representation of a sphere with 60 triangles; a regularly triangulated representation of a sphere with 1,500 triangles; an irregularly triangulated representation of a sphere with 1,440 triangles

triangles are used, the better becomes the approximation to the original "smooth" surface, as also seen in Fig. 1. We shall now describe the basic algorithm used to "triangulate" an arbitrarily shaped surface, with particular emphasis upon the extraction of an isosurface from the electronic density $\rho(\mathbf{r})$ of a molecule

The algorithm

Given a scalar function in three-dimensional real space, such as the electronic density $\rho(\mathbf{r})$ of an atomic or molecular system, an isosurface of the function at ρ_0 is defined by the equation $\rho(\mathbf{r})=\rho_0$. This is the basis for Bader et al.'s definition of a molecular surface [19].

Given a discrete sampling of an atomic or molecular density $\rho(\mathbf{r})$ on a three-dimensional grid, we follow several steps to extract an isodensity representation of a surface:

1. "Label" each grid point $\mathbf{r}_i = \{x_i, y_i, z_i\}$ with a 0 if $\rho(\mathbf{r}_i) > \rho_0$ ($\mathbf{r}_i$ is interior), and with a 1 otherwise ($\mathbf{r}_i$ is exterior or lies on the surface).
2. Any cube whose eight corners are either all labeled 0 (interior cube) or all 1 (exterior cube) is discarded. The remaining cubes have at least one interior corner and at least one exterior corner, and are thus intersected by the surface (and hereafter referred to as "surface cubes").
3. The surface within each "surface cube" is approximated by a finite number of triangles. This is done by following the next few steps:

   (a) Divide each cube into six tetrahedra
   (b) Discard the "exterior" and "interior" tetrahedra
   (c) For each "surface tetrahedron", find the intersection between the surface and its edges
   (d) Approximate the surface on each tetrahedron by either one or two triangles

Figure 2 shows a cubic 8×8×8 grid and a sphere embedded in it, which is defined by the equation $e^{-r^2} = e^{-\left(x^2+y^2+z^2\right)} = e^{-2.5^2} \approx 0.00193$, which corresponds to the ~0.00193 isosurface of an exponential centered at the origin. The MT algorithm is fed the values of e^{-r^2} at each point on the grid. After discarding all of the interior and exterior cubes, the surface within each surface cube is represented by triangles, as shown in Fig. 2. The way in which each surface patch in each cube is triangulated is what gives the MT algorithm its name, and distinguishes it from the MC algorithm: each surface cube is further divided into six tetrahedra, each of which can in turn intersect the surface or not. Figure 3 displays the orientation of the unit cube in real space, along with the numbering of its corners used in Table 1 to define the six tetrahedra. Since each of them has only four corners, there is a very limited number of different ways in which a tetrahedron can be intersected by a surface. These can be reduced by symmetry to only two, shown in Fig. 3, and corresponds to: (1) one triangle when the tetrahedron is formed by one interior (exterior) and three exterior (interior) grid points, and (2) two triangles when the tetrahedron is formed by two interior and two exterior grid points. The vertices of the triangles lie in a line joining an exterior and an interior grid point, and it follows that somewhere along that line the field takes on the value of the isosurface. The location of each triangle vertex can found by interpolation of corner values (or by any other appropriate means). We shall use both a linear and a cubic interpolation, deferring the details to a later section.

At this point, it is important to clarify some nomenclature. We use the word "cube" to refer to the minimum volume element defined by the grid, although it does not need to be a cube and can in fact be any parallelepiped. Each cube has eight "corners", which correspond of course to points in the grid. Whenever two adjacent corners have different labels (one is interior and the other exterior), there exists a "triangle vertex" (or simply "vertex" or "node") in the line that joins them, referred to as the "active segment". Each vertex belongs to a given number of triangles, and is thus joined by a line called "edge" to a certain number of other vertices. By "triangle," we shall mean an element of the surface that evidently is enclosed by three edges joining three vertices. Finally, each triangle shall have an assigned area and a center, given by its centroid. These data shall be used in the subsequent surface analysis.

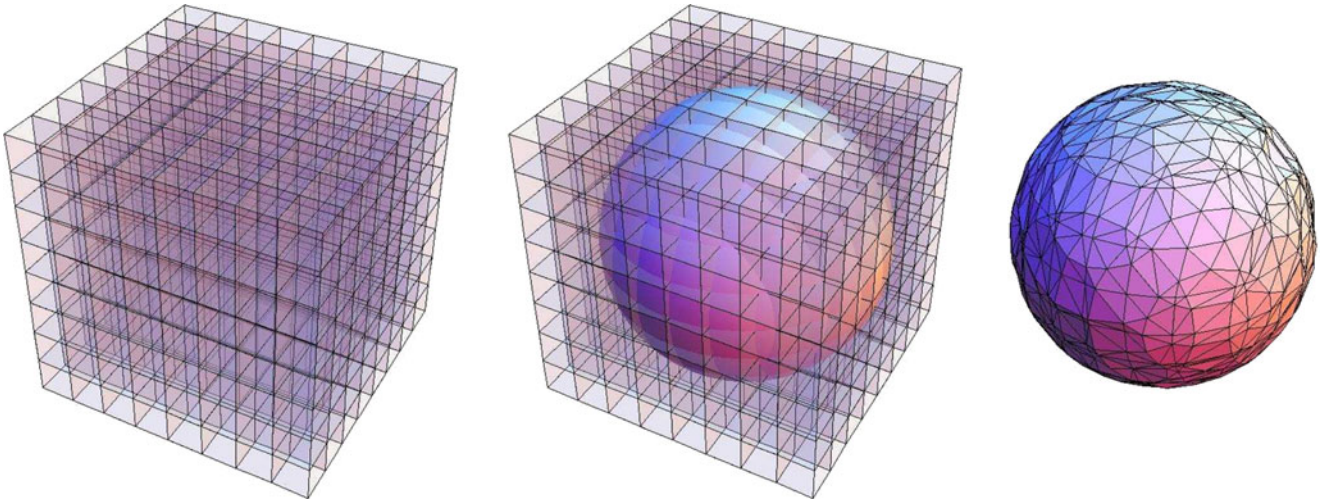

Fig. 2 From *left* to *right*: Cubic 8×8×8 grid; sphere embedded in the grid; triangulation of the sphere resulting from the application of the Marching Tetrahedra (MT) method with 1,656 triangles. The sphere is defined as the isosurface given by $e^{-r^2} = e^{-2.5^2} \approx 0.00193045$ (radius=2.5 a.u.), and the MT algorithm is fed with the values of the function e^{-r^2} at each point in the 8×8×8 regular grid

Our implementation

We briefly review the implementation details of the MT algorithm in our code (F.A.B. and A.T.-L., unpublished), emphasizing the elements important for the statistical analysis. Figure 4 displays the basic flow of the program and the subroutines into which the several loops are partitioned. The top-level routine MarchingCubesT receives the following input: the starting point $\mathbf{r}_{\text{ini}}$, the three vectors that define the regular grid $\Delta\mathbf{r}_i$, i=1,2,3, and the number of steps taken along each vector N_i=1,2,3. The grid thus correspond to a general regular grid, with unit volume $|\Delta\mathbf{r}_1 \cdot (\Delta\mathbf{r}_2 \times \Delta\mathbf{r}_3)|$. Each grid point has coordinates $\mathbf{r}_{ini} + \sum_{\ell=1}^{3} n_\ell \Delta\mathbf{r}_\ell$, where the n_l values correspond to the number of steps taken from $\mathbf{r}_{\text{ini}}$, and is identified with a triple $\{n_1,n_2,n_3\}$. A "layer" is generally defined as the collection of all points with a fixed value for any of the n_l, although here it will always mean the collections of points with fixed n_3. For our regular cubic grid, all points in a layer have the same z value. MarchingCubesT computes the electronic density (and $\bar{\mathrm{I}}(\mathbf{r})$ at no extra cost) for each layer, labels each grid point as exterior or interior, and passes two adjacent layers at a time to the next subroutine.

The DoTwoLayers subroutine simply takes the layer data passed by MarchingCubesT and loops over all cubes, calling the Cube6Tetra subroutine once per each surface cube, discarding internal and external cubes. The Cube6Tetra is the actual workhorse, and consists of two main loops, one over each tetrahedron per cube, and one over each pair of corners per tetrahedron. The latter identifies the surface

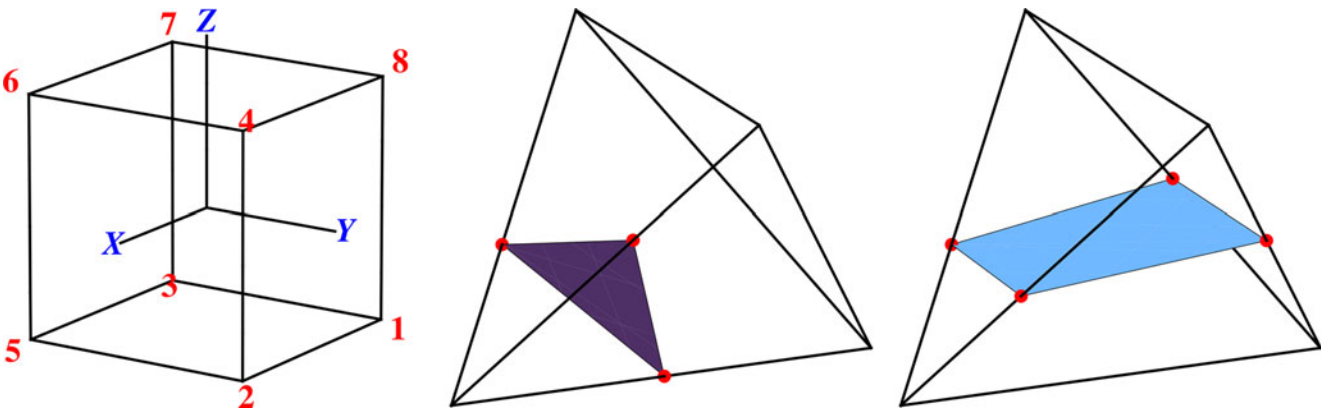

Fig. 3 From *left* to *right*: A given volume from which the isosurface will be extracted is first divided into a uniform grid, such as that seen in Fig. 2, whose basic unit is represented schematically here as a cube (*left*). The convention for numbering the corners of the cube is shown relative to the coordinate axes. Each cube on the grid is subsequently divided into six tetrahedra, which are defined by six sets of four cube corners as shown in Table 1. The intersection of the surface and a surface tetrahedron can define one (*middle*) or two (*right*) triangles

Table 1 The four vertices of the six tetrahedra into which each cube in the grid is divided. The numbering of the vertices corresponds to that shown in Fig. 3

Tetrahedron	Vertices			
1	3	2	1	8
2	3	2	4	8
3	3	7	4	8
4	3	4	5	2
5	3	4	5	7
6	6	4	5	7

tetrahedra and discards all other types (exterior and interior), proceeding then to the computation of the triangle vertices and area. The point at which the surface intersects each active segment, i.e. the vertex position $\mathbf{r}_c^v$, is found by

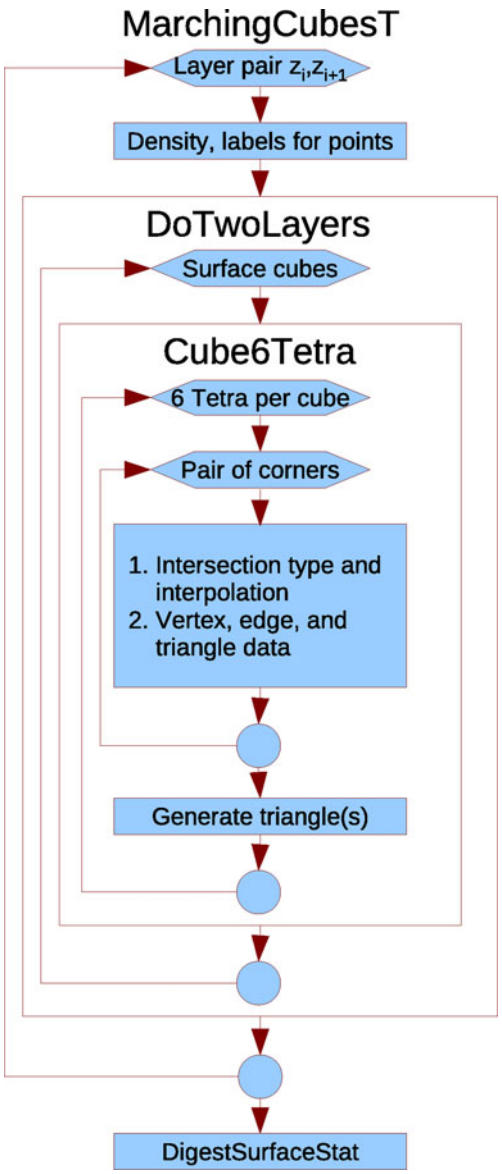

Fig. 4 Flow chart showing the basic subroutines into which the tasks are divided. See text for details

interpolation between the two corners a and b. For reasons that we will discuss later, both linear and cubic interpolation schemes have been implemented. The linear interpolation requires no further data since it only uses the density values $\rho(\mathbf{r}_a)$ and $\rho(\mathbf{r}_b)$:

$$\mathbf{r}_c^v = \mathbf{r}_a + \eta\ \mathbf{r}_b \tag{7}$$

$$\text{where}: \eta = \frac{\rho(\mathbf{r}_a) - \rho_0}{\rho(\mathbf{r}_a) - \rho(\mathbf{r}_b)} \tag{8}$$

whereas the cubic interpolation requires two additional calls (one per corner) to a routine that evaluates the density and its derivatives $\{\rho(\mathbf{r}_\ell), \nabla\rho(\mathbf{r}_\ell)\}$. The function $\rho(\mathbf{r}(t)) - \rho_0$, with $\mathbf{r}(0)=\mathbf{r}_a$ and $\mathbf{r}(1) = \mathbf{r}_b$, is approximated by a cubic function using the density values $\rho(\mathbf{r}_a)$ and $\rho(\mathbf{r}_b)$ and the directional derivatives:

$$\rho'_{ab}(t) = \frac{\partial\rho(\mathbf{r}(t))}{\partial t} = \frac{\nabla\rho(\mathbf{r}) \cdot \{\mathbf{r}_b - \mathbf{r}_a\}}{|\mathbf{r}_b - \mathbf{r}_a|} \frac{\partial\mathbf{r}(t)}{\partial t} \tag{9}$$

which simplify to:

$$\rho'_{ab}(t) = \frac{\partial\rho(\mathbf{r}(t))}{\partial t} = \nabla\rho(\mathbf{r}) \cdot \{\mathbf{r}_b - \mathbf{r}_a\} \tag{10}$$

because $\frac{\partial\mathbf{r}(t)}{\partial t} = |\mathbf{r}_b - \mathbf{r}_a|$ for our choice of the mapping $\mathbf{r}(t)$. The factor η entering Eq. 7 is then determined by solving the following cubic equation:

$$a + b\eta + c\eta^2 + d\eta^3 = 0, \forall\eta \parallel 0 < \eta < 1 \tag{11}$$

where:

$$\begin{aligned} a &= \rho(\mathbf{r}_a) - \rho_0 \\ b &= \rho'_{ab}(0) \\ c &= -3a - 2b + 3[\rho(\mathbf{r}_b) - \rho_0] - \rho'_{ab}(1) \\ d &= 2a + b - 2[\rho(\mathbf{r}_b) - \rho_0] + \rho'_{ab}(1) \end{aligned} \tag{12}$$

After the vertices for each surface tetrahedron have been computed, Cube6Tetra determines the area of the triangle or triangles, depending on whether the surface intersects the tetrahedron at three or four points (as in Fig. 3). The triangle and vertex data are stored in individual linked lists. After completion of the main loop in the top level routine MarchingCubesT, the surface is complete, and we save the coordinates of all vertices, the values of any fields of interest such as V(**r**), and a list of all the triangles as a triple of vertex indices (their numbers on the vertex list). Note that some fields, such as $\bar{\mathrm{I}}(\mathbf{r})$, are computed along with the density (at no extra cost), so their values are known at the

cube corners. To obtain their values at the vertices we use an interpolation procedure similar to that used to obtain the position of the vertex along the active segments. For fields that are not computed along with the density (and are usually more expensive), such as V(**r**), we compute the values at the vertices after the surface has been constructed. Because the number of vertices is much smaller than the number of grid points, this procedure is significantly more efficient for such fields. At this stage, the surface construction is now complete, and we shall proceed to describe the methods used for the statistical analyses.

Surface analyses

For a surface S defined by $\rho(\mathbf{r})=\rho_0$, the total surface area A, internal volume V, and surface average $\overline{f}_S$ of a field $f(\mathbf{r})$ can be defined as:

$$\begin{aligned} A_S &= \int\int_S dS \\ V_S &= \int\int\int_{\Omega_S} d\mathbf{r} \\ \overline{f}_S &= \tfrac{1}{A_S}\int\int_S f(\mathbf{r})dS \end{aligned} \tag{13}$$

In practice, A_S is simply the sum of all the areas of the N_t triangles that represent the surface, while V_S is the sum of the volumes of all internal cubes, plus the volume of the internal parts of the surface cubes. The average $\overline{f}_S$ could be computed as:

$$\overline{f}_S \approx \frac{\sum_{t=1}^{all} f(\mathbf{r}_t)A(t)}{A_S} \tag{14}$$

Where $A(t)$ is the area of the t-th triangle. Indeed, this could be generalized so that any quantity defined as a surface average could be computed as a sum over triangles:

$$\overline{\mathrm{F}}_S[f(\mathbf{r})] = \frac{1}{A_S}\int\int_S \mathrm{F}[f(\mathbf{r})]dS \approx \frac{\sum_{t=1}^{all}\mathrm{F}[f(\mathbf{r}_t)]A(t)}{A_S} \tag{15}$$

However, we have found in practice that the following alternative working formula works equally well:

$$\overline{\mathrm{F}}_S[f(\mathbf{r})] \approx \frac{\sum_{t=1}^{all}\mathrm{F}[f(\mathbf{r}_t)]}{N_t} \tag{16}$$

All of the quantities defined by Eqs. 3–5 can be treated in this manner.

We are also interested in determining the local surface extrema of fields $f(\mathbf{r})$ such as $\mathrm{V_S}(\mathbf{r})$ and $\overline{\mathrm{I}}_\mathrm{S}(\mathbf{r})$. This is achieved by comparing the value of the each vertex to that of all other vertices in a simply connected neighborhood. Neighborhoods can be defined through either distance or connectivity, i.e., all points within a given distance from the reference point (R_n-neighbors) or all points connected through no more than n edges to the reference point (n-neighbors). If a given reference point is smaller (larger) than all the other points in the neighborhood, then it is identified as a local minimum (maximum). We have seen that connectivity neighborhoods are very effective in identifying surface extrema, and we use 2-neighborhoods in all our calculations. The computation of the 2-neighborhoods can be fairly time-consuming and, to keep the computational requirements to a minimum, we first identify "candidate vertices" by initially screening the 1-neighborhoods. This is usually enough to rule out most vertices, and we then perform the full comparison against all 2-neighbors on this reduced subset of all "candidates", which speeds up the process significantly.

The triangle vertices that define the surface can lie slightly inside or slightly outside the actual $\rho(\mathbf{r})=\rho_0$ surface. Furthermore, it sometimes occurs that a given vertex lies slightly outside the surface (at $\rho_0+\delta$) while all of its neighbors lie slightly inside the surface (at $\rho_0-\delta$). Combined with the fact that some fields (like $\overline{\mathrm{I}}(\mathbf{r})$) can vary slowly in regions of the surface, some vertices are wrongly identified as local extrema. This is the reason that the cubic interpolation scheme was included as an alternative to the linear, as it significantly improves the accuracy of finding the position of the vertex along the active segment, and reduces the occurrence of false surface extrema to a minimum. As an indicator of how closely the vertices lie to the exact surface, we use their root-mean-square deviation (RSMD):

$$RMSD(\rho) = \sqrt{\frac{\sum_{i=1}^{N_v}\left[\rho(\mathbf{r}_i)-\rho_0\right]^2}{N_v}} \tag{17}$$

RMSD(ρ) is typically one order of magnitude smaller when the cubic interpolation is used instead of the linear.

Results

We will present several applications of our analysis algorithm to illustrate its performance. We first examine the computation of volume and surface area in terms of the sphere in Fig. 2. We then move on to the volumes, surface areas and statistical characterization of the molecular surface electrostatic potentials and local ionization energies of a group of 11 molecules. An important feature of our procedure is that it can locate and evaluate the extrema of $\mathrm{V_S}(\mathbf{r})$ and $\overline{\mathrm{I}}_\mathrm{S}(\mathbf{r})$, and we shall discuss these in relation to graphical representations of $\mathrm{V_S}(\mathbf{r})$ and $\overline{\mathrm{I}}_\mathrm{S}(\mathbf{r})$ for 3 of the 11 molecules.

Table 2 Calculated volume and surface area using a cubic interpolation, and root mean squares deviation RMSD(ρ) using both cubic and linear interpolations for a sphere defined by $e^{-r^2} = e^{-2.5^2} \approx 0.00193045$ (radius=2.5 a.u.) as in Fig. 2. The errors in the estimation of volume and surface area are shown. All values are in atomic units

Length of side	Number of triangles	Volume	%Error	Surface area	% Error	RMSD(ρ)	
						Cubic	Linear
0.650	1,656	63.653	−2.74	78.920	0.48	0.316×10^{-3}	0.876×10^{-3}
0.480	3,088	64.552	−1.37	78.260	−0.36	0.130×10^{-3}	0.576×10^{-3}
0.325	6,624	65.125	−0.50	78.373	−0.21	0.0448×10^{-3}	0.318×10^{-3}
0.230	13,376	65.305	−0.22	78.461	−0.10	0.0199×10^{-3}	0.167×10^{-3}
0.130	41,832	65.405	−0.07	78.516	−0.03	0.0610×10^{-4}	0.556×10^{-4}
0.065	166,968	65.440	−0.02	78.534	−0.01	0.0144×10^{-4}	0.145×10^{-4}

Representation of a sphere

Table 2 shows the number of triangles used to describe the surface of the sphere with different cubic grids ranging from the 8×8×8 grid used in Fig. 2, corresponding to a spacing (cube side) of 0.650 a.u., to an 80×80×80 grid with a spacing ten times smaller (0.065 a.u.). The number of triangles grows quickly with the decreasing grid spacing, going from 1,656 to 166,968 when the spacing is reduced from 0.650 a.u. to 0.065 a.u. The errors in the integrated surface area and the volume it encloses also decrease rapidly, by two orders of magnitude (Table 2), which parallels the increase in the number of triangles used in the surface representation. However, even for the largest grid spacing of 0.650 a.u., the errors in the integrated volume and surface area are quite small, amounting to −2.7% and 0.5%, respectively. Table 2 also shows that RMSD(ρ) improves greatly with smaller grid spacing. As mentioned above, when the cubic interpolation is used, RMSD(ρ) is one order of magnitude less than for the linear, for all grid spacings ≤0.325 a.u.

Molecular analyses

Molecular volume has long been of interest because of its relationship to polarizability [1–3]; quite recently, it has also assumed a key role in estimating two important properties of energetic compounds: their crystal densities [4–7] and their impact sensitivities [8]. Accordingly, an initial test of our implementation in the WFA program was for predicting the molecular volumes of a group of five energetic compounds [47]: Tetryl (**1**), RDX (**2**), TNAZ (**3**), N,N′-dinitro-1,2-diaminoethane (**4**) and FOX-7 (**5**).

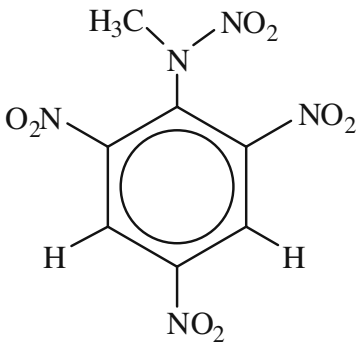

1

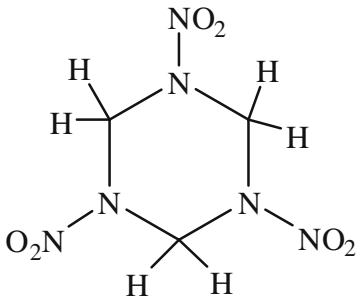

2

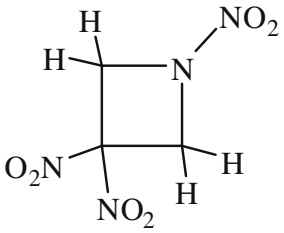

3

$O_2N\text{-}NH\text{-}CH_2\text{-}CH_2\text{-}NH\text{-}NO_2$

4

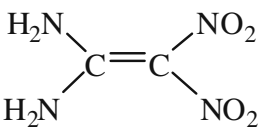

5

Table 3 lists the molecular volumes of these five compounds, as defined by the 0.001 a.u. contours of their electronic densities. For the surface construction, we use a cubic grid with a spacing of 0.20 a.u. (0.11 Å). The volumes were computed at the density functional B3PW91/6-31G(d,p) and B3LYP/6-31G(d,p) levels. Gaussian 03 [48] was used to obtain the optimized geometries and wavefunction files, from which our WFA program calculated the volumes. For comparison, Table 3 also contains the volumes determined by Rice et al. [49] by means of a Monte Carlo technique. The three sets of results are very similar. The Monte Carlo/B3LYP volumes are slightly larger than the WFA/B3LYP, but only by an average of 0.4%. The latter are in turn larger than the WFA/B3PW91 by an average 0.6%. So the WFA and the Monte Carlo volumes are in excellent agreement, as are the WFA with the different functionals. (Volumes corresponding to other contours of the electronic density can also be obtained using WFA.)

We also used WFA to compute a wide array of properties on the 0.001 a.u. surfaces of **1**–**5** plus a group of six additional molecules of different chemical types: H_2O, phenol, SCl_2, dimethyl sulfoxide (DMSO, **6**), acetone (**7**), and imidazole (**8**).

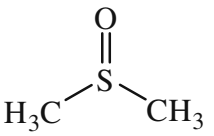

6

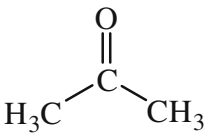

7

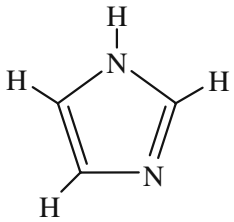

8

Table 4 includes, for each of the 11 molecules, the positive, negative and total surface areas (A_S^+, A_S^- and A_S), the average positive, negative and overall surface potentials ($\overline{V}_S^+$, $\overline{V}_S^-$ and $\overline{V}_S$), the positive, negative and total variances (σ_+^2, σ_-^2 and σ_{tot}^2), the internal charge separation Π, the balance parameter ν and the average over the surface of the local ionization energy $\overline{I}_{S,ave}$. All of these properties were computed by WFA, in a single run for each molecule, utilizing B3PW91/6-31G(d,p) optimized geometries, wave functions and electrostatic potential cube files from Gaussian 03.

There are a number of points of interest in Table 4. The positive and negative surface areas are similar for most of the molecules, the two exceptions being DMSO (**6**) and acetone (**7**) and for which $A_S^+ >> A_S^-$. This is because a large portion of the surface is taken up by the positive methyl hydrogens. Note, however, that while the oxygens in these molecules occupy only a small fraction of each surface, their strongly negative electrostatic potentials lead to $\overline{V}_S^-$ having twice the magnitude of $\overline{V}_S^+$, and $\sigma_-^2 >> \sigma_+^2$, for each molecule.

H_2O has the greatest internal charge separation, Π= 23.91 kcal mol^{-1}, followed closely by FOX-7, **5**. This is not surprising, given their obviously highly polar structures. Less expected, perhaps, are the high Π values of **2** and **4**, which are structurally more symmetric. These examples demonstrate the significance of Π, which detects the high level of charge separation produced *internally* in these molecules by the NO_2 groups.

Note that while the positive and negative surface potentials of H_2O are strong, as seen in its $\overline{V}_S^+$ and $\overline{V}_S^-$, they are quite well balanced: ν=0.249. In contrast, the much weaker surface potentials in SCl_2 have a low degree of balance, ν=0.064.

The largest σ_{tot}^2 in Table 4 is that of FOX-7, **5**. It indicates strong and variable positive and negative surface potentials, which are a consequence of the donor/acceptor natures of the NH_2/NO_2 substituents and are associated

Table 3 Computed molecular volumes, in $Å^3$

Molecule	WFA	WFA	Monte Carlo
	B3PW91/6-31(d,p)	B3LYP/6-31G(d,p)	B3LYP/6-31G(d,p)[a]
1	263.55	265.03	266.49
2	203.61	205.05	206.28
3	176.29	177.48	178.05
4	154.03	155.04	155.47
5	140.51	140.83	141.27

[a] [49]

Table 4 Computed molecular surface properties[a]. *DMSO* Dimethyl sulfoxide

Molecule	A_S	A_S^+	A_S^-	$\overline{V}_S$	$\overline{V}_S$	$\overline{V}_S^-$	σ^2_{tot}	σ^2_+	σ^2_-	Π	ν	$\overline{I}_{S,ave}$
Tetryl, **1**	249.5	136.2	113.3	5.31	18.85	−10.75	140.1	104.9	35.2	15.11	0.188	13.27
RDX, **2**	197.8	97.6	100.2	3.54	23.22	−15.49	181.3	139.9	41.4	19.45	0.176	13.27
TNAZ, **3**	181.0	93.3	87.7	4.89	19.16	−9.58	161.5	131.2	30.3	14.77	0.152	13.49
$(CH_2NHNO_2)_2$, **4**	165.7	87.3	78.4	3.65	22.93	−17.84	250.4	191.4	59.0	20.44	0.180	12.82
FOX-7, **5**	149.5	75.9	73.6	1.52	25.05	−22.11	453.3	351.5	101.8	23.60	0.174	11.44
Phenol	133.4	64.8	68.5	0.16	11.87	−11.25	165.3	124.0	41.3	11.56	0.187	11.40
DMSO, **6**	115.2	79.8	35.4	1.75	13.95	−26.07	277.7	31.0	246.8	16.99	0.099	11.44
Acetone, **7**	106.6	77.4	29.2	1.72	10.52	−21.35	167.9	25.9	142.0	12.78	0.131	11.88
SCl_2	105.5	53.9	51.6	2.16	7.03	−2.90	39.2	36.5	2.7	5.27	0.064	11.24
Imidazole, **8**	102.6	52.2	50.5	0.25	17.32	−17.76	336.1	174.2	161.9	17.53	0.250	11.50
H_2O	42.9	21.4	21.5	0.74	24.68	−23.12	290.1	155.9	134.2	23.91	0.249	12.07

[a] Units: A_S, A_S^+ and A_S^- are in Å^2; $\overline{V}_S$, $\overline{V}_S^+$, $\overline{V}_S^-$ and Π are in kcal mol^{-1}; σ^2_{tot}, σ^2_+ and σ^2_- are in (kcal mol^{-1})2; ν is unitless; $\overline{I}_{S,ave}$ is in eV

especially with the NH_2 hydrogens and NO_2 oxygens. A consequence is the extensive intermolecular hydrogen bonding in crystalline FOX-7, which helps to account for its relatively high density [7].

In Figs. 5, 6 and 7 are displayed the $V_S(\mathbf{r})$ and $\overline{I}_S(\mathbf{r})$ on the 0.001 a.u. surfaces of phenol, Tetryl (**1**) and SCl_2. The figures show the locations of the various most positive and most negative $V_S(\mathbf{r})$, designated $V_{S,max}$ and $V_{S,min}$, and the highest and lowest $\overline{I}_S(\mathbf{r})$, $\overline{I}_{S,max}$ and $\overline{I}_{S,min}$, as shown in Figs. 5, 6 and 7. There are often several local maxima and minima of each property on a given molecular surface, all of which are located and quantified by the WFA code.

Figure 5 provides a good example of the complementarity of $V_S(\mathbf{r})$ and $\overline{I}_S(\mathbf{r})$, discussed earlier. The most negative electrostatic potential on the phenol surface is associated with the oxygen, $V_{S,min}$=−25.9 kcal mol^{-1}, with two weaker ones of −19.1 kcal mol^{-1} above and below the ring, reflecting the π electrons. Thus, $V_S(\mathbf{r})$ would incorrectly predict electrophilic attack to occur preferentially at the oxygen. In contrast, the lowest values of $\overline{I}_S(\mathbf{r})$ are above and below the ortho and para carbons, with $\overline{I}_{S,min}$ = 8.9 eV; there is also an $\overline{I}_{S,min}$ by the oxygen, but it is much higher, 10.6 eV. Thus, $\overline{I}_S(\mathbf{r})$ shows the most reactive, least-tightly-bound electrons to be at the ortho and para positions, correctly indicating these sites to be most susceptible to electrophiles. Furthermore, since the $\overline{I}_{S,min}$ of 8.9 eV are less than those found for benzene at this computational level (9.2 eV), $\overline{I}_S(\mathbf{r})$ is demonstrating the well-known activation of the ring by the hydroxyl group. On the other hand, the very strongly positive electrostatic potential of the hydroxyl hydrogen, $V_{S,max}$=54.1 kcal mol^{-1}, and the $V_{S,min}$=−25.9 kcal mol^{-1} of the oxygen indicate their propensities for noncovalent hydrogen bonding, as a donor and an acceptor, respectively.

The key structural elements of Tetryl (**1**)—its aromatic ring, nitro groups and nitramine (N–NO_2) grouping—give rise to a number of $V_S(\mathbf{r})$ and $\overline{I}_S(\mathbf{r})$ extrema (Fig. 6). We will emphasize just two points: (1) the regions of negative

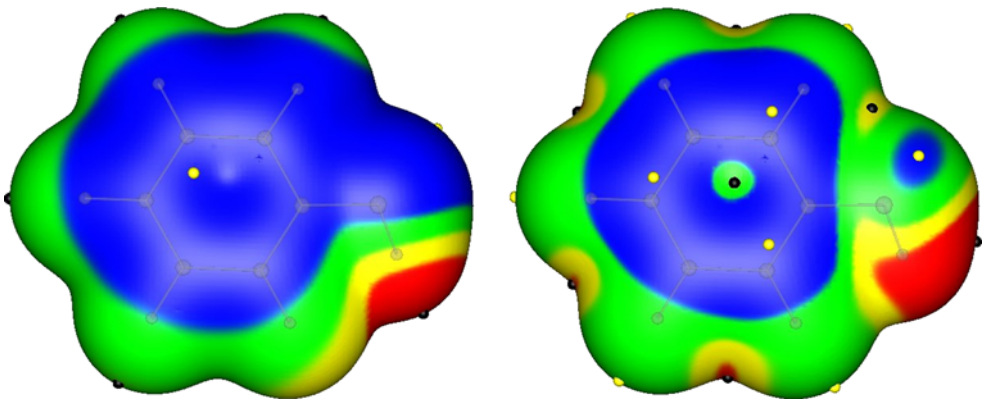

Fig. 5 Calculated $V_S(\mathbf{r})$ (*left*) and $\overline{I}_S(\mathbf{r})$ (*right*) of phenol. In each plot, the hydroxyl group is at the right. Color ranges for $V_S(\mathbf{r})$, in kcal mol^{-1}: *red* > 31.4, *yellow* 31.4–15.7, *green* 15.7–0.0, *blue* < 0 (negative). Color ranges for $\overline{I}_S(\mathbf{r})$, in eV: *red* > 13.6, *yellow* 13.6–12.2, *green* 12.2–10.9, *blue* < 10.9. *Black circles* Surface maxima, *yellow* surface minima. The most negative $V_S(\mathbf{r})$ is associated with the oxygen, $V_{S,min}$=−25.9, while the lowest $\overline{I}_S(\mathbf{r})$, $\overline{I}_{S,min}$ = 8.9, are over the ortho and para carbons

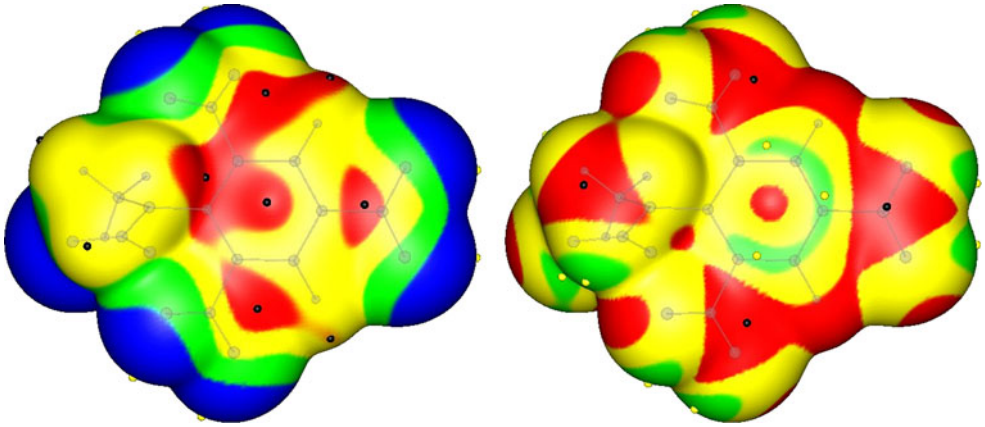

Fig. 6 Calculated $V_S(\mathbf{r})$ (*left*) and $\bar{I}_S(\mathbf{r})$ (*right*) of Tetryl (**1**). In each plot, the nitramino group is at the left (with its methyl group in the foreground). Color ranges for $V_S(\mathbf{r})$, in kcal mol^{-1}: *red* > 31.4, *yellow* 31.4–15.7, *green* 15.7–0.0, *blue* < 0 (negative). Color ranges for $\bar{I}_S(\mathbf{r})$, in eV: *red* > 13.6, *yellow* 13.6–12.2, *green* 12.2–10.9, *blue* < 10.9. *Black circles* Surface maxima, *yellow* surface minima. For $\bar{I}_S(\mathbf{r})$, only maxima with values greater than 15.6 eV and minima with values less than 12.2 eV are shown. There are strongly positive $V_S(\mathbf{r})$ regions above the ring and near the C–NO_2 bonds

potential normally produced above and below aromatic rings by the π electrons (see Fig. 5) have been completely eliminated by the presence of the three strongly electron-withdrawing NO_2 ring substituents; these regions are now entirely positive. (2) There is an unusual buildup of positive electrostatic potential, with a local $V_{S,max}$, near each C–NO_2 bond. This is not normally observed for covalent bonds, but it has been found as well in nitroaliphatics and in nitroheterocycles. Both of these features have been linked to the impact sensitivities of these classes of energetic compounds [50–52].

The molecular surface electrostatic potential of SCl_2, in Fig. 7, illustrates the occurrence of positive σ-holes, also mentioned in a previous section. The two S–Cl bonds are formed through the interactions of two half-filled sulfur bonding orbitals with a half-filled orbital on each chlorine. Since the electronic charge in each of these half-filled orbitals is polarized toward the bonding region, there is a deficiency in its outer, noninvolved lobe. This gives rise to a region of positive electrostatic potential on the outer side of that atom, on the extension of the covalent bond to it (a positive σ-hole). Two such positive regions can be seen on the sulfur and one on each chlorine, on the extensions of the S–Cl bonds (Fig. 7). Each can interact attractively with a negative site on another molecule, albeit rather weakly in the case of the chlorines, which have $V_{S,max}$ of only 13.3 kcal mol^{-1} compared to 25.2 kcal mol^{-1} for the two σ-holes on the sulfur.

The sulfur and the chlorines in SCl_2 also have regions of negative potential on their surfaces, as well as their positive σ-holes. This means, for example, that a sulfur from one SCl_2 molecule can interact attractively with a sulfur from another; S–S close contacts in sulfur-containing solids have indeed been observed crystallographically [53]. This also

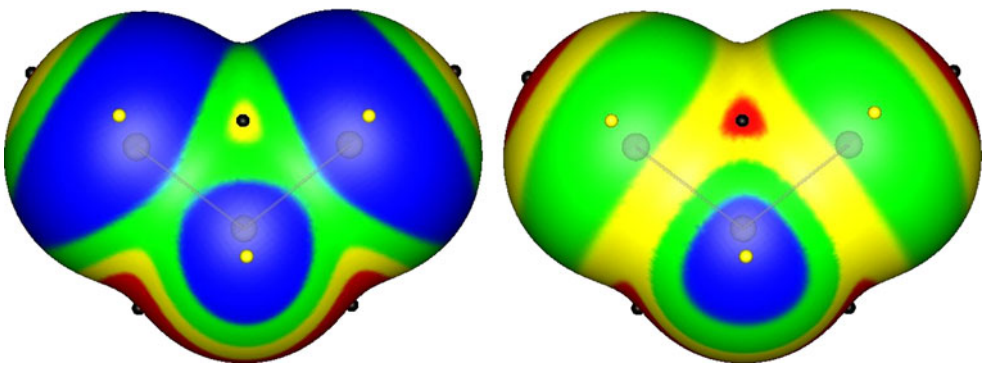

Fig. 7 Calculated $V_S(\mathbf{r})$ (*left*) and $\bar{I}_S(\mathbf{r})$ (*right*) of SCl_2. In each plot, the sulfur is at the bottom. Color ranges for $V_S(\mathbf{r})$, in kcal mol^{-1}: *red* > 12.6, *yellow* 12.6–6.3, *green* 6.3–0.0, *blue* < 0 (negative). Color ranges for $\bar{I}_S(\mathbf{r})$, in eV: *red* > 12.2, *yellow* 12.2–11.2, *green* 11.2–9.8, *blue* < 9.8. *Black circles* Surface maxima, *yellow* surface minima. There are two positive σ-holes on the sulfur, $V_{S,max}$=25.2, on the extensions of the Cl–S bonds, and one on each chlorine, $V_{S,max}$=13.3, on the extenstion of the S–Cl bond. The sulfur and the chlorines also have regions of negative $V_S(\mathbf{r})$ on their sides

demonstrates the fallacy of assigning global charges to atoms in molecules, a point to be kept in mind when designing force fields [54, 55].

Note, in Fig. 7, that the $\bar{I}_{S,max}$ of the sulfur and the chlorines coincide with their positive σ-holes. This is reasonable; the more positive the $V_S(\mathbf{r})$, the more difficult it should be to remove an electron, and hence the higher $\bar{I}_S(\mathbf{r})$. However, this approximate correlation between $V_S(\mathbf{r})$ and $\bar{I}_S(\mathbf{r})$ is not always found, as can be seen from the example of phenol: the oxygen has the most negative $V_{S,min}$, but a higher $\bar{I}_{S,min}$ than the carbons. Another example of a sulfur σ-hole is in DMSO (**6**), which has a $V_{S,max}$ of 26.4 kcal mol^{-1} on the extension of the O–S bond. With a strongly negative oxygen $V_{S,min}$ of −46.0 kcal mol^{-1} and the positive methyl hydrogens, this molecule has several opportunities for intermolecular interactions [56], which helps to explain its well known effectiveness as a solvent.

Concluding remarks

We have described the development and implementation of an effective algorithm for analyzing properties evaluated on molecular surfaces. Our primary focus has been upon electrostatic potentials and average local ionization energies; the quantitative characterization of these on molecular surfaces provides considerable insight and predictive capability concerning interactive behavior. We would like to emphasize, however, that the method is general and an effective tool to analyze quantitatively any field defined over a molecular surface.

Our implementation is based upon the Marching Tetrahedra approach, but can be applied in conjunction with any representation of a three-dimensional surface as a collection of polygons. We have implemented this procedure in the WFA program , which is available from the author (F.A.B.) along with: (1) the graphical user interface gWFA to set up the WFA input files for the surface generation and statistical analysis, and (2) a simple visualization tool, SurRender (used to obtain Figs. 5, 6, and 7)

Acknowledgments J.S.M. and P.P. appreciate the support of the Defense Threat Reduction Agency, Contract No. HDTRA1-07-1-0002, Project Officer Dr. William Wilson.

References

1. Laidig KE, Bader RFW (1990) J Chem Phys 93:7213–7224
2. Brinck T, Murray JS, Politzer P (1993) J Chem Phys 98:4305–4306
3. Jin P, Murray JS, Politzer P (2006) Int J Quantum Chem 106:2347–2355, and references therein
4. Murray JS, Brinck T, Politzer P (1996) Chem Phys 204:289–299
5. Rice BM, Hare JJ, Byrd EFC (2007) J Phys Chem A 111:10874–10879
6. Qiu L, Xiao H, Gong X, Ju X, Zhu W (2007) J Hazard Mat 141:280–288
7. Politzer P, Martinez J, Murray JS, Concha MC, Toro-Labbé A (2009) Mol Phys 107:2095–2101
8. Pospíšil M, Vávra P, Concha MC, Murray JS, Politzer P (2009) J Mol Model, doi:10.1007/s00894-009-0587-x
9. Lee B, Richards FM (1971) J Mol Biol 55:379–400
10. Weinter PK, Langridge R, Blaney JM, Schaefer R, Kollman PA (1982) Proc Natl Acad Sci USA 79:3754–3758
11. Connolly ML (1983) Science 221:709–713
12. Francl MM, Hout RF Jr, Hehre WJ (1984) J Am Chem Soc 106:563–570
13. Arteca GA, Jammal VB, Mezey PG, Yadov JS, Hermsmeier MA, Gund TM (1988) J Mol Graph 6:45–53
14. Dunitz JD, Filippini G, Gavezzotti A (2000) Tetrahedron 56:6595–6601
15. Bondi A (1964) J Phys Chem 64:441–451
16. Brickmann J, Exner T, Keil M, Marhöfer R, Moeckel G (1998) In: Schleyer PvR (ed) Encylopedia of computational chemistry, vol 3. Wiley, New York, pp 1678–1693
17. Connolly ML (1998) In: Schleyer PvR (ed) Encylopedia of computational chemistry, vol 3. Wiley, New York, pp 1698–1703
18. Bader RFW, Henneker WH, Cade PE (1967) J Chem Phys 46:3341–3363
19. Bader RFW, Carroll MT, Cheeseman JR, Chang C (1987) J Am Chem Soc 109:7968–7979
20. Murray JS, Lane P, Politzer P (2009) J Mol Model 15:723–729
21. Murray JS, Brinck T, Grice ME, Politzer P (1992) J Mol Struct THEOCHEM 256:29–45
22. Brinck T, Murray JS, Politzer P (1992) Mol Phys 76:609–617
23. Politzer P, Murray JS (2009) Croatica Chim Acta 82:267–275
24. Stewart RF (1979) Chem Phys Lett 65:335–342
25. Politzer P, Truhlar DG (eds) (1981) Chemical applications of atomic and molecular electrostatic potentials. Plenum, New York
26. Sjoberg P, Murray JS, Brinck T, Politzer P (1990) Can J Chem 68:1440–1443
27. Koopmans TA (1934) Physica 1:104–113
28. Politzer P, Abu-Awwad F, Murray JS (1998) Int J Quantum Chem 69:607–613
29. Bulat FA, Levy M, Politzer P (2009) J Phys Chem A 113:1384–1389
30. Toro-Labbé A, Jaque P, Murray JS, Politzer P (2005) Chem Phys Lett 407:143–146
31. Politzer P, Murray JS, Concha MC (2002) Int J Quantum Chem 88:19–27
32. Feynman RP (1939) Phys Rev 56:340–343
33. Hirschfelder JO, Curtiss CF, Bird RB (1954) Molecular theory of gases and liquids. Wiley, New York
34. Naray-Szabo G, Ferenczy GG (1995) Chem Rev 95:829–847
35. Sjoberg P, Brinck T (1991); Brinck T (1995) HardSurf program
36. Hagelin H, Brinck T, Berthelot M, Murray JS, Politzer P (1995) Can J Chem 73:483–488
37. Riley KE, Murray JS, Politzer P, Concha MC, Hobza P (2009) J Chem Theor Comput 5:155–163
38. Murray JS, Brinck T, Lane P, Paulsen K, Politzer P (1994) J Mol Struct THEOCHEM 307:55–64
39. Politzer P, Murray JS (1998) J Mol Struct THEOCHEM 425:107–114
40. Murray JS, Politzer P (1998) In: Schleyer PvR (ed) Encyclopedia of computational chemistry, vol 2. Wiley, New York, pp 912–920
41. Politzer P, Murray JS (2001) Fluid Phase Equil 185:129–137
42. Politzer P, Murray JS (2007) In: Toro-Labbé A (ed) Chemical Reactivity, Elsevier, Amsterdam, pp 119–137

43. Politzer P, Murray JS, Bulat FA (2010) J Mol Model. doi:10.1007/s00894-010-0709-5
44. Lorensen WE, Cline HE (1987) SIGGRAPH 163–169
45. Payne BA, Toga AW (1990) IEEE Comput Graph Appl 10:33–41
46. Chan SL, Purisima EO (1998) J Comput Chem 19:1268–1277
47. Meyer R, Köhler J, Hornburg A (2007) Explosives, 6th edn. Wiley-VCH, Weinheim, Germany
48. Frisch MJ et al (2004) Gaussian 03, Revision C.02. Gaussian Inc, Wallingford, CT
49. Rice BM, Hare JJ, Byrd EFC (2007) J Phys Chem A 111:10874–10879
50. Murray JS, Lane P, Politzer P (1998) Mol Phys 93:187–194
51. Rice BM, Hare JJ (2002) J Phys Chem A 106:1770–1783
52. Murray JS, Concha MC, Politzer P (2009) Mol Phys 107:89–97
53. Guru Row TN, Parthasarathy R (1981) J Am Chem Soc 103:477–479
54. Auffinger P, Hays FA, Westhof E, Shing Ho P, Van Holde KE (2004) Proc Nat Acad Sci USA 101:16789–16794
55. Politzer P, Murray JS, Concha MC (2008) J Mol Model 14:659–665
56. Clark T, Murray JS, Lane P, Politzer P (2008) J Mol Model 14:689–697